

Brittle and ductile failure constraints of stress-based topology optimization method for fluid–structure interactions



Gil Ho Yoon

School of Mechanical Engineering, Hanyang University, Seoul, Republic of Korea

ARTICLE INFO

Article history:

Received 7 December 2016

Received in revised form 5 April 2017

Accepted 22 April 2017

Available online 19 May 2017

Keywords:

Topology optimization

Brittle material

Ductile material

Stress-based topology optimization

Fluid–structure interaction

Monolithic approach

ABSTRACT

This study considers failure theories for brittle and ductile materials in the stress-based topology optimization method (STOM) for steady state fluid–structure interactions (FSI). In some relevant studies, the subject of the stress-based topology optimization to minimize volumes with local von Mises stress constraints has been researched. However, the various failure theories for ductile and brittle materials, such as the maximum shear stress theory, the brittle and ductile Mohr–Coulomb theory, and the Drucker–Prager theory, have not been considered. For successful STOM for FSI, in addition to alleviating physics interpolation issues between structure and fluid and some numerical issues related to STOM, the mathematical characteristics of the various failure theories should be properly formulated and constrained. To resolve all the involved computational issues, the present study applies the monolithic analysis method, the qp -relaxation method, and the p -norm approach to the failure constraints. The present topology optimization method can create optimal layouts while minimizing volume constraining local failure constraints for ductile and brittle materials for steady state fluid and structural interaction system.

© 2017 Elsevier Ltd. All rights reserved.

1. Introduction

The multiphysics simulation of fluid–structure interactions (FSI) is an important subject for a very wide variety of scientific and engineering applications. Computational complications in the involved physical theories have introduced novel ideas based on in-depth understanding toward physics and many numerical analysis procedures. Depending on differences in the manner of computational coupling between fluids and structures, these analysis procedures can be categorized as either staggered or monolithic analysis procedures (see [1,2] and references therein). Additionally, many studies can be found with regard to size and shape structural optimization methods for FSI systems, and there are some topology optimization studies for topological alternations or connectivity alternations inside FSI domains [2–9]. Furthermore, it is rare to consider brittle and ductile failure constraints in topology optimization for FSI [10–12]. To contribute to this topic, this study presents a new STOM method with the various failure constraints for FSI systems in corporation with the monolithic approach, qp -relaxation methods, and the p -norm approach.

Despite many topology optimization studies for a variety of engineering topics, few studies can be found for topology optimization for FSI systems. In [2], the theoretical difficulties with regard to applying existing analysis methods for FSI systems for topology optimization were discussed, and a monolithic approach was proposed for topology optimization. The study was extended to consider the mutual couplings among electric, fluid, thermal, and structures in [7]. Afterward, the monolithic procedure was extended to consider the local stress constraints for topology optimization in [13]. On the other hand, various numerical approaches have been proposed [5,7,14–17]. In [4,5], topology optimization for laminar and turbulent

E-mail addresses: gilho.yoon@gmail.com, ghy@hanyang.ac.kr.

<http://dx.doi.org/10.1016/j.camwa.2017.04.015>

0898-1221/© 2017 Elsevier Ltd. All rights reserved.

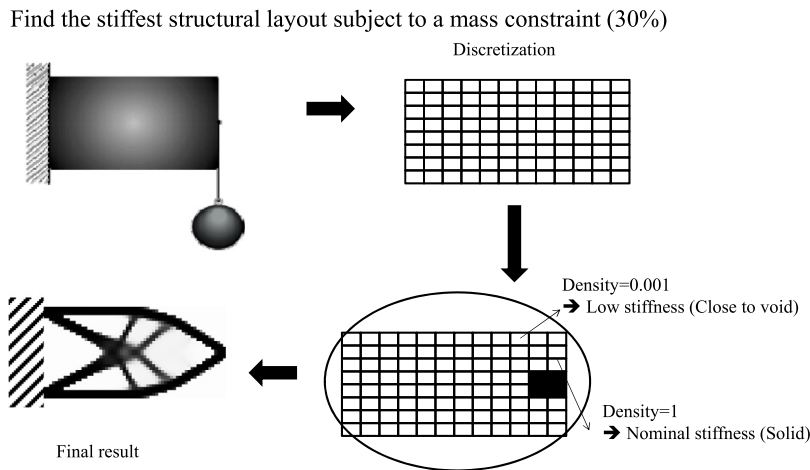


Fig. 1. Structural topology optimization practice.

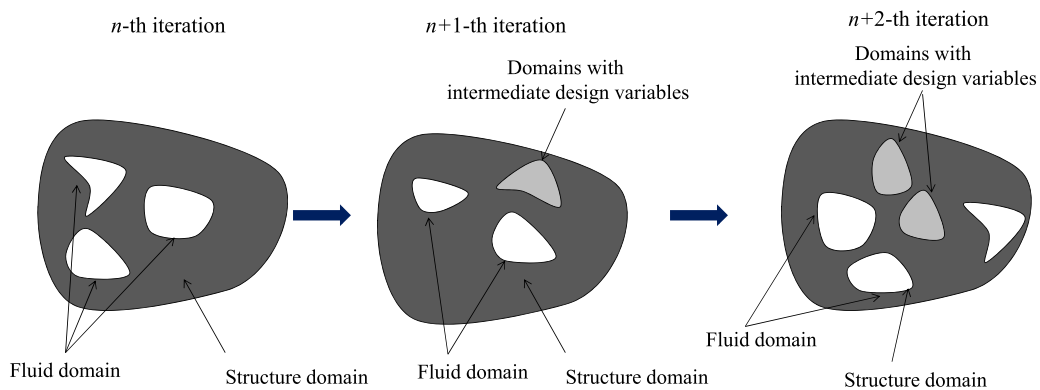


Fig. 2. Interpolating equations governing fluid and structure interactions.

flow including heat transfer was carried out. In [8], optimal shape designs were presented for a subsonic intake geometry using aerodynamic sensitivity analysis. In [15,16], some industrial optimization applications in electronic devices were presented. A saturated poroelastic actuator and FSI problem in the poroelasticity of shock absorbers were considered in [18,19]. Also, the reliability shape optimization methods were developed in [3]. In [20], the high-fidelity aero structure design method was proposed to reduce computational costs. In [14], a topology optimization method for the optimal flow channels in micro-mixers using the Boltzmann method while neglecting structural deformations was proposed. With standard FSI analysis methods, topology optimization was carried out for internal aircraft wing structures in [6] with high speed parallel algorithms. Turbulent effects were considered in [4,5,21] with the Spalart–Allmaras turbulent model. Furthermore, it was possible to discover many relevant studies for FSI, acoustic, and fluid problems in TO [6,19,22–27]. The shape optimization methods were developed in FSI in [3,20]. Furthermore, in an earlier study performed by our group [13], the von Mises stress constraints were considered in the STOM for FSI structures after resolving many theoretical and numerical issues [28–45]; in the present study, various failure theories for ductile and brittle materials are considered. Also there are some researches using the mixed formulation utilizing the displacement and the stress independently to improve the accuracy [42,45].

Issues of topology optimization (TO) for fluid–structure interactions

For a successful STOM for FSI system, several issues related to the multiphysics systems should be addressed [13]. Unlike purely structural topology optimization, some complicated and unclear points exist for topology optimization simulation procedures of the multiphysics system when optimizing the spatially varying density variables in Fig. 1. First, it is not clear how to interpret the two governing equations with regard to intermediate density design variables in Fig. 2. Due to this ambiguity, the state-of-the-art staggered or monolithic analysis methods for FSI systems developed to date have some difficulties to apply to STOM problems with ductile and brittle failure criteria. To overcome these difficulties, relevant researches have adopted monolithic analysis for FSI [2,7,46]. One of the most important differences between our monolithic analysis and the existing numerical analyses is that the linear structural equation and Navier–Stokes equation are governed at unified analysis and design domains. In our monolithic approach, the interaction–coupling boundary conditions are satisfied by modeling domain forces for the continuity of traction and clamp conditions for the continuity of fluidic velocity illustrated in Fig. 3. This monolithic analysis approach was applied toward structural optimization problems, including the

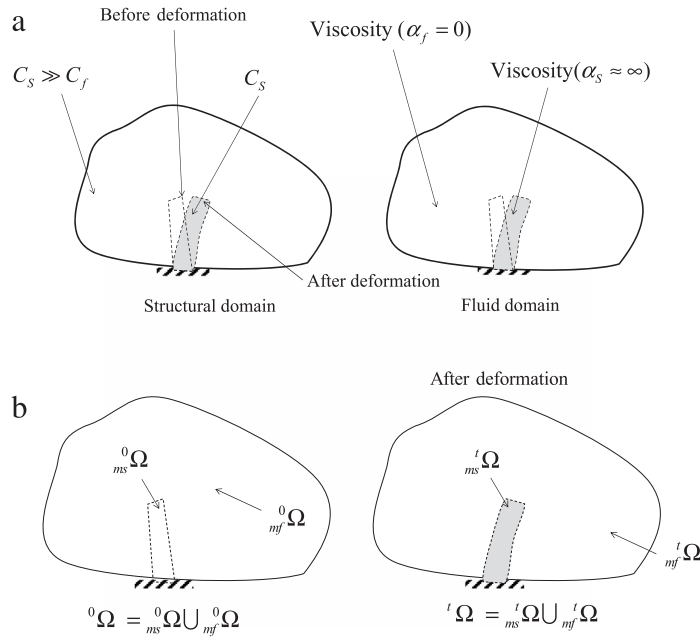


Fig. 3. Monolithic analysis in our prior research [2,7,13]: material properties for structures and fluids (where the Young's moduli of the structure and fluid are C_s and C_f , respectively, and the inverse coefficients of solid and fluid permeability are α_s and α_f , respectively).

STOM with local von Mises stress constraints in our prior research [2,13]. The present research also employs the monolithic analysis approach for the STOM with ductile and brittle failure constraints.

Three issues related to stress based topology optimization methods

Besides the three issues related to the interpolation of FSI multiphysics systems, some theoretical issues related to the STOM should be properly addressed with regard to failure constraints for brittle and ductile materials [28–38], i.e., singularity issues, element stress constraint issues, and highly nonlinear constraint issues. With regard to the singularity issue, the present study adopts the qp -relaxation method using different penalty parameters for constitutive matrices for the forward FE analysis and the stress analysis with respect to the SIMP (Solid Isotropic Material with Penalization) design variables [39–44]. To overcome the issue of many local stress constraints, the present study adopts an aggregation function called the p -norm approach [28–38,47,48]. Highly nonlinear stress constraint behaviors need to be addressed too [49,50]. To resolve these issues, the prior knowledge accumulated from the aforementioned studies, and various numerical approaches are implemented.

This paper is organized as follows: Section 2 describes the basic equations for the FSI multiphysics systems. In Section 3, the development of the present STOM formulation is described. Section 4 presents several numerical examples to show the advantages and disadvantages of the present STOM procedure with the various failure criteria. Section 5 presents the conclusions and suggests future research topics.

2. A monolithic FE formulation for FSI systems

This section briefly reviews the employed monolithic approach in [2,7,13]. To alleviate the aforementioned complications in the density based topology optimization method for FSI, the finite deformation tensor is introduced to formulate the coupled multiphysics equations and to consider continuous morphological changes to fluid and structural domains [2,7,13]. In continuum mechanics, the finite deformation tensor \mathbf{F} is defined as the partial differentiation of the current coordinate \mathbf{x} with respect to the undeformed coordinate, \mathbf{X} . This deformation tensor can be used to correlate the differential operators and the integral operators of the undeformed and deformed configurations as well as the physical quantities of the two configurations, such as mass density, strain, and volume, as (1)–(4).

$$\mathbf{x} = \mathbf{X} + \mathbf{u}, \quad \mathbf{F} = \frac{\partial \mathbf{x}}{\partial \mathbf{X}} \quad (1)$$

$$\text{Differential Operators : } \nabla_{\mathbf{x}} = \mathbf{F}^T \nabla_{\mathbf{X}}, \quad \nabla_{\mathbf{X}} = \mathbf{F}^{-T} \nabla_{\mathbf{x}} \quad (2)$$

$$\text{Integral Operators : } \int_{\Omega} (\cdot) d\Omega = \int_{{}^0\Omega} (\cdot) \|\mathbf{F}\| d\Omega \quad (3)$$

$${}^0\Omega = {}^0\Omega_{ms} \cup {}^0\Omega_{mf}, \quad {}^t\Omega = {}^t\Omega_{ms} \cup {}^t\Omega_{mf}. \quad (4)$$

The undeformed fluid domain (${}^0_{mf}\Omega$) and the undeformed solid domain (${}^0_{ms}\Omega$) domains are defined within the undeformed domain, ${}^0\Omega$. The deformed fluid domain (${}^t_{mf}\Omega$) and the deformed solid domain (${}^t_{ms}\Omega$) are defined inside the deformed domain, ${}^t\Omega$. In the employed monolithic formulation, the fluid equation for fluid velocity and pressure at the deformed domain ${}^t\Omega$ can be redefined in the undeformed domain, ${}^0\Omega$.

$$-\int_{{}^0\Omega} \delta \mathbf{v}^T \{ \rho (\mathbf{v} \cdot \mathbf{F}^{-T} \nabla_{\mathbf{x}} \mathbf{v}) \} \|\mathbf{F}\| d\Omega = \int_{{}^0\Omega} \mathbf{F}^{-T} \nabla_{\mathbf{x}} \delta \mathbf{v}^T \mathbf{T}_f \|\mathbf{F}\| d\Omega + \int_{{}^0\Omega} \alpha \delta \mathbf{v}^T \mathbf{v} \|\mathbf{F}\| d\Omega - \int_{{}^0\Gamma_{p^*}} p_{p^*} \mathbf{n} d\Gamma \quad (5)$$

$$-\int_{{}^0\Omega} \delta p^T \{ (\nabla_{\mathbf{x}} \cdot \mathbf{v}) \} \|\mathbf{F}\| d\Omega = 0 \quad (6)$$

$$\mathbf{T}_f = -p\mathbf{I} + \mu(\nabla_{\mathbf{x}} \mathbf{v} + \nabla_{\mathbf{x}} \mathbf{v}^T) \quad (7)$$

$$\text{No-slip boundary condition : } \mathbf{v} = \mathbf{0} \quad \text{on } {}^t_f\Gamma_{v^0}(\mathbf{u}) \quad (8)$$

$$\text{Inflow/outflow boundary condition : } \mathbf{v} = \mathbf{v}^* \quad \text{on } {}^t_f\Gamma_{v^*}(\mathbf{u}) \quad (9)$$

$$\text{Interfacing boundary condition : } \mathbf{v} = \frac{d\mathbf{u}}{dt} (\equiv \mathbf{0} \text{ for steady state flow}) \quad \text{on } {}^t_f\Gamma_i(\mathbf{u}) \quad (10)$$

$$\text{Pressure boundary condition : } \mathbf{T}_f \cdot \mathbf{n} = p_{p^*} \mathbf{n} \quad \text{on } {}^t_f\Gamma_{p^*}(\mathbf{u}). \quad (11)$$

See [2,7] for the verifications of the above formulation with comparisons to the existing staggered analysis method. The fluid velocity field and pressure are denoted by \mathbf{v} and p , respectively, and the fluid density and dynamic viscosity for Newtonian flow are denoted by ρ and μ , respectively. The Dirichlet boundary conditions are prescribed along ${}^t_f\Gamma_{v^0}$. The inflow/outflow boundary conditions and the interfacing boundary condition are defined along ${}^t_f\Gamma_{v^*}$, and ${}^t_f\Gamma_i(\mathbf{u})$, respectively. With the normal vector \mathbf{n} , the Neumann boundary condition for applied pressure p_{p^*} is defined at ${}^t_f\Gamma_{p^*}(\mathbf{u})$; the boundary before the deformation is defined along ${}^0\Gamma_{p^*}$. The inverse coefficient of fluid permeability, used for the asymptotic simulation of zero velocity fluid motion for solid domains in topology optimization, is α . With a sufficiently large value of α , the fluidic velocity approaches zero for the structural domains and at the coupling boundary.

As the external elastic energy due to fluid stress at the coupling boundary is also dependent on structural displacements, the deformation tensor can be applied after applying the divergent theory in (12):

$$\int_{{}^0\Omega} \delta \mathbf{S}^T \cdot \mathbf{T}_s d\Omega = \int_{{}^0\Omega} \Psi \cdot \mathbf{F}^{-T} \delta \mathbf{S}(\mathbf{u}, \delta \mathbf{u})^T \cdot p \|\mathbf{F}\| d\Omega + \int_{{}^0\Omega} \Psi \cdot \mathbf{F}^{-T} \delta \mathbf{u} \cdot \nabla_{\mathbf{x}} p \|\mathbf{F}\| d\Omega \quad (12)$$

$$\mathbf{S} = \frac{1}{2}(\nabla_{\mathbf{x}}^T \mathbf{u} + \nabla_{\mathbf{x}} \mathbf{u}), \quad \mathbf{T}_s = \mathbf{C} \mathbf{S} \quad (13)$$

$$\mathbf{S}(\mathbf{u}, \delta \mathbf{u}) = \frac{1}{2}(\nabla_{\mathbf{x}}^T \mathbf{u} + \nabla_{\mathbf{x}} \delta \mathbf{u}), \quad \nabla_{\mathbf{x}} = \mathbf{F}^{-T} \nabla_{\mathbf{X}} \quad (14)$$

where the linear strain \mathbf{S} and the associate stress \mathbf{T}_s are defined as above. The linear constitutive matrix is denoted by \mathbf{C} . The scalar function Ψ is 1 and 0 for solid and fluid domains, respectively. By solving (5) and (6) for fluids and (12) for solids, the fluid–structure interaction system can be analyzed successfully; see [2,7,13] for more details.

The qp -relaxation method and interpolation functions of the SIMP method

To avoid the stress singularity, this study adopts the qp -relaxation approach which uses the different penalization factors for the SIMP method as follows:

$$\text{Forward analysis : } \mathbf{C}_e = \gamma_e^n (\mathbf{C}_s - \mathbf{C}_f) + \mathbf{C}_f \quad (15)$$

$$\text{Stress analysis : } {}_s\mathbf{C}_e = \gamma_e^{n_s} (\mathbf{C}_s - \mathbf{C}_f) + \mathbf{C}_f \quad (16)$$

where the penalization factors for forward analysis and stress analysis are n and n_s , respectively. To overcome the singularity issue, 5 is used for n and 0.5 is used for n_s . The density design variable assigned for the e th element is γ_e . The constitutive matrices of the e th finite element for the forward analysis and the stress analysis are denoted by \mathbf{C}_e and ${}_s\mathbf{C}_e$, respectively, with \mathbf{C}_s and \mathbf{C}_f for constitutive matrices of solid and fluid, respectively. Additionally, the auxiliary functions are interpolated similarly.

$$\Psi = \gamma_e^{n_{filter}} \quad (17)$$

$$\alpha(\gamma_e) = \alpha_{\max} \gamma_e^{n_{per}}. \quad (18)$$

The maximum inverse permeability is denoted by α_{\max} and the penalty factors of the fluid pressure filter and the inverse permeability are denoted by n_{filter} and n_{per} , respectively.

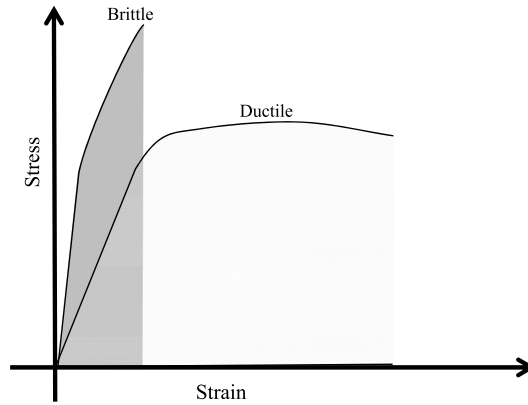


Fig. 4. Stress and strain curve for ductile and brittle materials (ductile materials: extensive plastic deformation and energy absorption prior to fracture; brittle materials: little plastic deformation and low energy absorption prior to fracture).

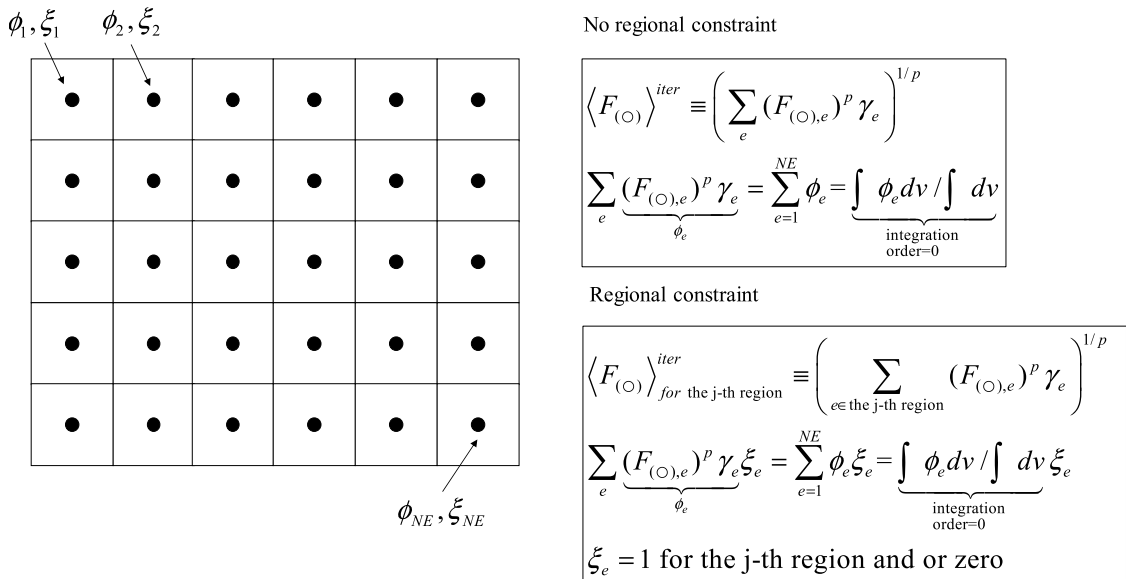


Fig. 5. Sensitivity analysis and regional constraint.

3. Stress based topology optimization formulation with ductile and brittle failure criteria

3.1. Ductile and brittle materials

Fracture phenomena of a solid structure are subjective by the fundamental characteristics of a solid. Brittle fracture can be defined as the growth of crack due to accumulated elastic energy inside a solid system. It shows little plastic deformation and low energy absorption before fracture. For other cases, ductile fracture is defined with extensive plastic deformation and energy absorption before fracture. Without existing cracks of critical size fracture, a material is always first ductile. When the stress at the crack mouth reaches the value of theoretical strength, i.e., Griffith's criterion $\sigma_c = \sqrt{\frac{2E\gamma_s}{\pi a}}$ with specific surface energy γ_s , Young's modulus E and crack size a , material becomes brittle. Common stress strain curves for ductile fracture and brittle fracture are presented in Fig. 4.

3.2. Failure criteria for topology optimization

Many failure criteria exist to predict the failures of solid structures. For structural topology optimization, this research considers the distortion energy theory, the maximum shear stress theory, the brittle and ductile Coulomb–Mohr theory, and the Drucker–Prager theory.

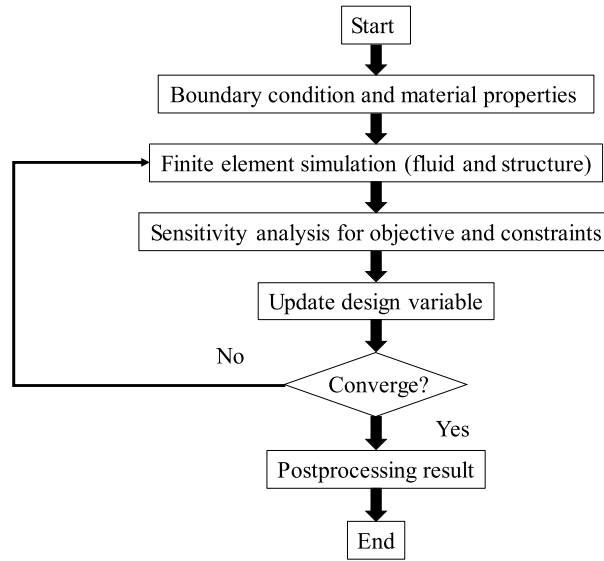


Fig. 6. Optimization process.

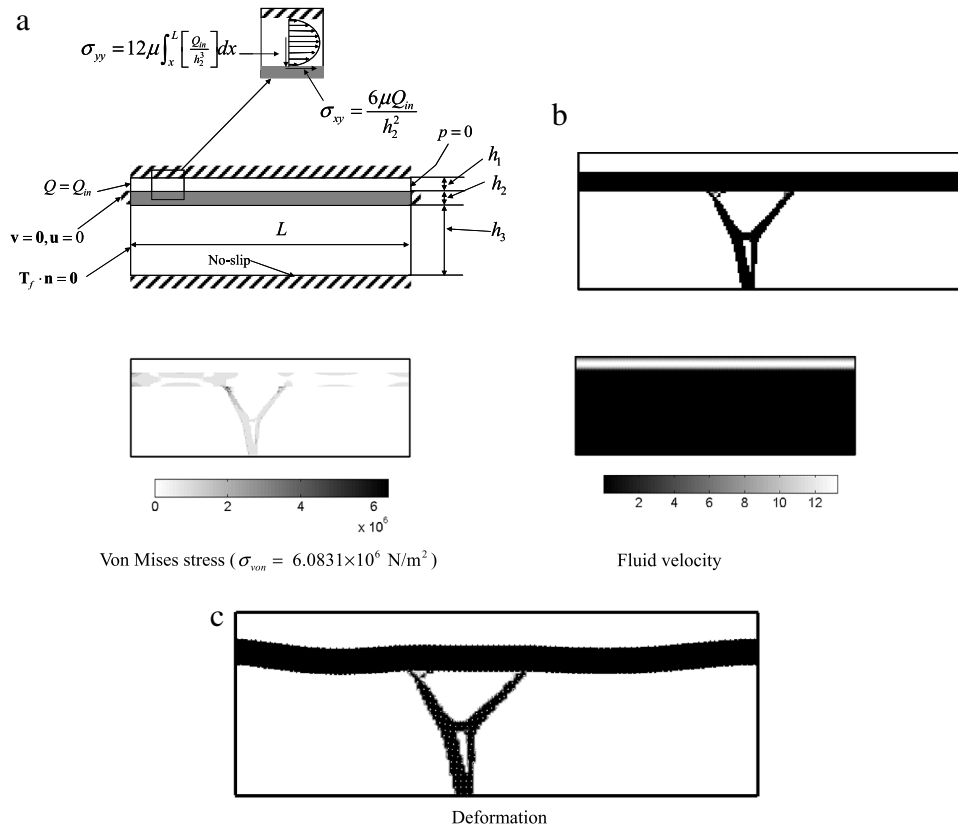


Fig. 7. A beam problem. (a) A plain-strain model with flow (Reynolds number = 240, $Q_{in} = 177 \times 10^{-6} \text{ m}^3 \text{ s}^{-1}$, $L = 4 \cdot 10^{-4} \text{ m}$, $h_1 = 2 \cdot 10^{-5} \text{ m}$, $h_2 = 2 \cdot 10^{-5} \text{ m}$, $h_3 = 1 \cdot 10^{-4} \text{ m}$, $\rho = 1000 \text{ kg/m}^3$, $\mu = 0.001 \text{ kg m}^{-1} \text{ s}^{-1}$, $E = 3 \times 10^{11} \text{ N/m}^2$, $\nu = 0.3$), (b) an optimal layout for compliance (5% Mass, Max von Mises $\sigma_{von} = 6.0831 \times 10^6 \text{ N/m}^2$, Compliance of the horizontal bar = $5.6669 \times 10^{-9} \text{ J}$), and (c) von Mises stress, fluid velocity and deformation.

Distortion Energy (DE) theory (von Mises criterion)

The von Mises criterion may be the most well-known criterion for material failure and has been mainly considered in structural topology optimization due to its simplicity and its differentiability with regard to the stress components and the design variables [10,11]. In the assumption of the DE theory, a failure occurs when the distortion strain energy per unit

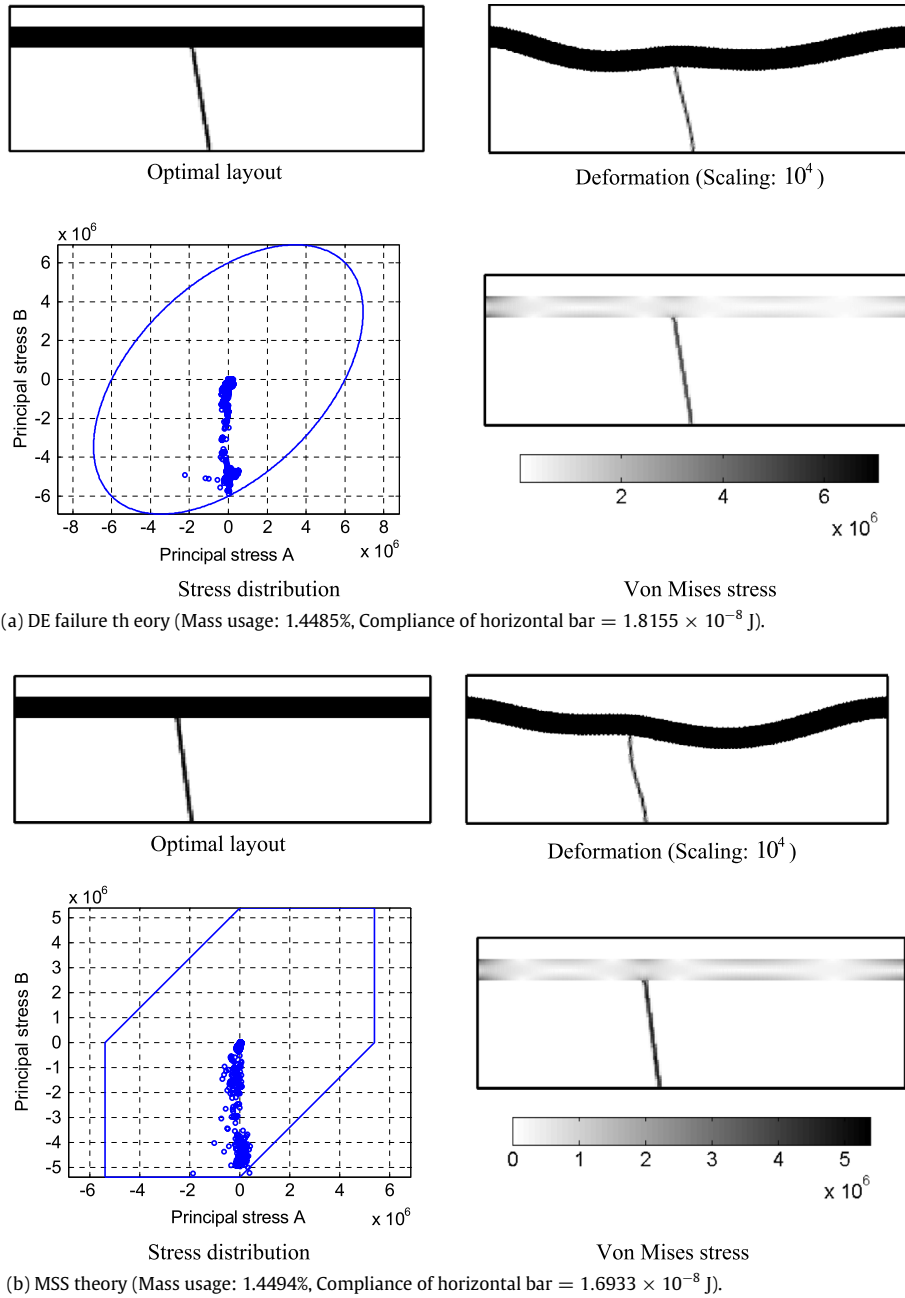


Fig. 8. Optimization results using the DE failure theory (movelimit = 0.1) and the MSS failure theory (movelimit = 0.05) (initial design variable = 0.3, $S_y = 6.0 \times 10^6$ N/m²).

volume exceeds the strain energy of a yielded unit volume in simple tension or compression tests, which can be described as follows:

$$F_{DE}(\sigma) = \frac{\sigma_v}{S_y} = \frac{\sqrt{3J_2(\sigma)}}{S_y} \leq 1. \quad (19)$$

The yield stress is denoted by S_y . The second invariant of the stress tensor and von Mises stress are denoted by J_2 and σ_v ,

$$J_2(\sigma) = \frac{(\sigma_{xx} - \sigma_{yy})^2 + (\sigma_{yy} - \sigma_{zz})^2 + (\sigma_{zz} - \sigma_{xx})^2 + 6\sigma_{xy}^2 + 6\sigma_{yz}^2 + 6\sigma_{zx}^2}{6} \quad (20)$$

$$\sigma_v = \sqrt{3J_2} = \sqrt{\frac{(\sigma_1 - \sigma_2)^2 + (\sigma_2 - \sigma_3)^2 + (\sigma_3 - \sigma_1)^2}{2}} \quad (21)$$

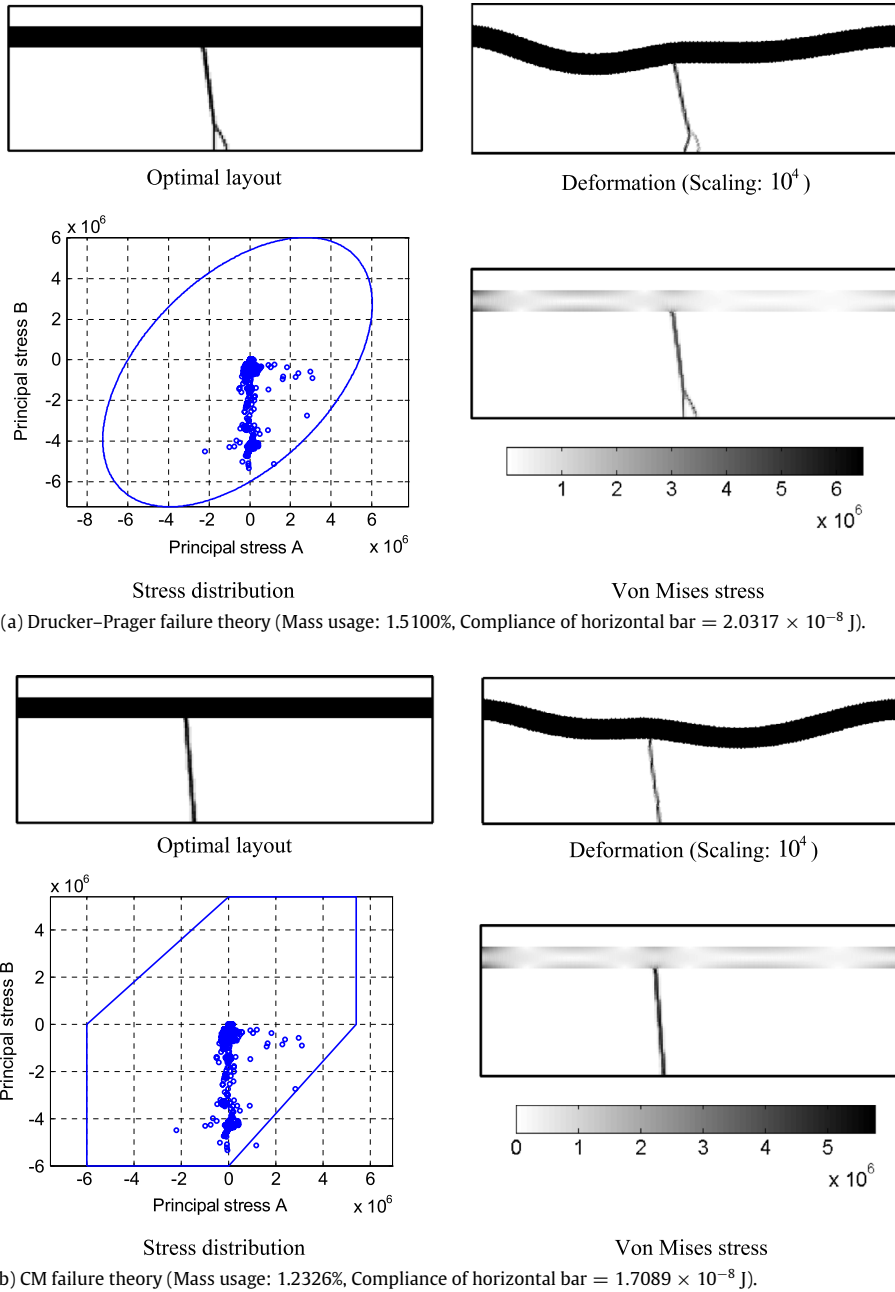


Fig. 9. Optimization results using the Drucker–Prager failure theory (movelimit = 0.1) and the CM failure theory (movelimit = 0.1) (Initial design variable = 0.3, $S_c = 6.0 \times 10^6$ N/m², $S_t = 5.4 \times 10^6$ N/m²).

where $\sigma = [\sigma_{xx}, \sigma_{yy}, \sigma_{zz}, \sigma_{xy}, \sigma_{yz}, \sigma_{zx}]$ is the stress of a material point. The principal stresses are σ_1, σ_2 and σ_3 . The yield surface is defined by $F_{DE}(\sigma) = 0$. As the envelope of the failure criterion is smooth, the differentiability issue does not exist.

Maximum-shear stress (MSS) theory (Tresca theory)

The fracture behaviors in tensile test specimens can be described by the MMS theory. The MSS formulation is based on the maximum and minimum values of the three principal stresses and consequently, its criterion is non-differentiable with respect to both the design variables as well as the principal stress components of topology optimization.

$$F_{MMS_Original}(\sigma) = \frac{\max(\sigma_1, \sigma_2, \sigma_3) - \min(\sigma_1, \sigma_2, \sigma_3)}{S_y} \leq 1. \quad (22)$$

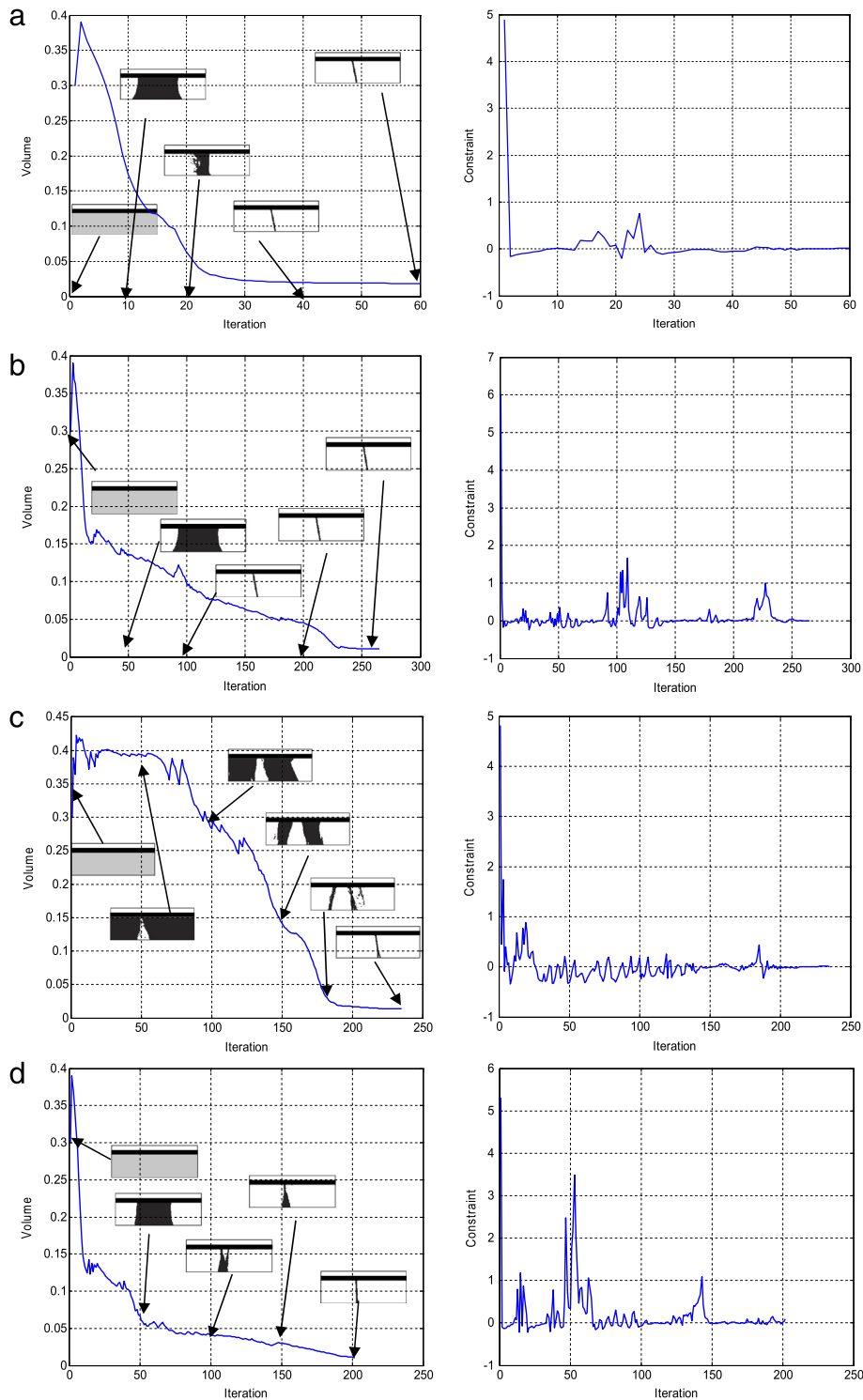


Fig. 10. Optimization histories of the first examples.

The maximum and the minimum values of the principal stress values are denoted by $\max(\sigma_1, \sigma_2, \sigma_3)$ and $\min(\sigma_1, \sigma_2, \sigma_3)$, respectively. As the operators are not differentiable, the differentiable max and min operators for STOM should be adopted [31].

By combining the pseudo max operators, the following maximum and the minimum operators for the three variables, a , b , and c , are used:

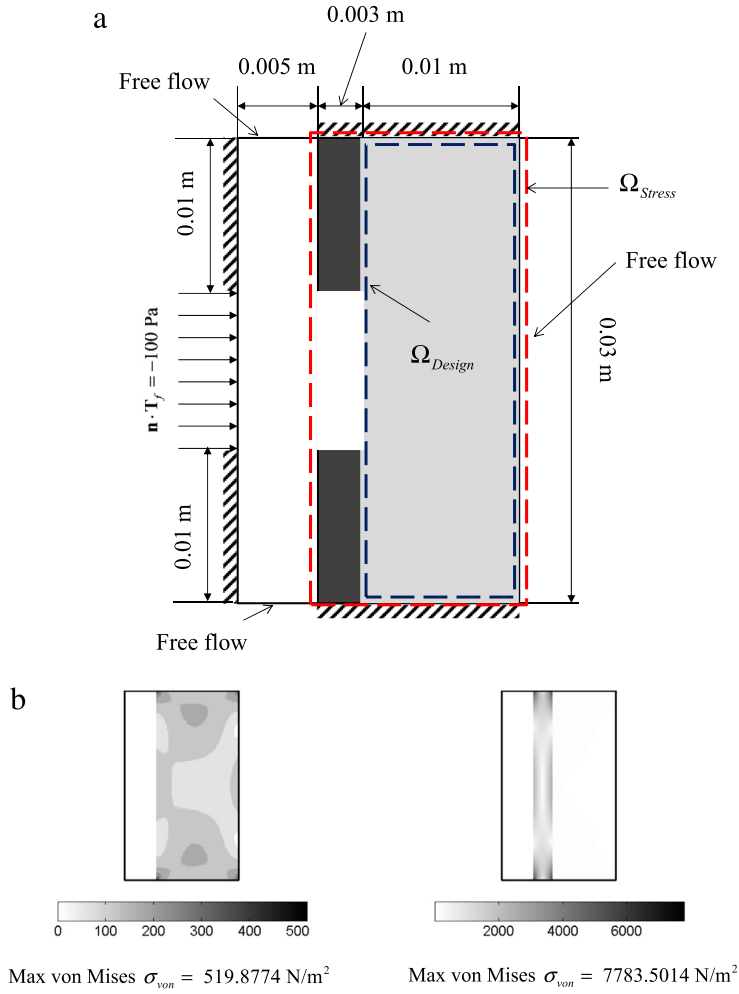


Fig. 11. STOM problem definitions with the pressure input at the center slot on the right (Reynolds number = 5, $\rho = 1000 \text{ kg/m}^3$, $\mu = 1.002 \text{ Pa s}$, $C_s = 10\,000 \text{ N/m}^2$, $\nu = 0.31$, $C_f = C_s \times 10^{-6} \text{ N/m}^2$, $\alpha_{\max} = 10^9$, element size: 1.6666×10^{-4} by 1.6666×10^{-4} or mesh: 108×180 , objective domain: Ω_{Stress} , design domain: Ω_{Design}).

$$\begin{aligned} \Psi_{\max}(a, b, c) &= \frac{a}{4} + \frac{b}{4} + \frac{c}{2} + \frac{\sqrt{(a-b)^2 + \varepsilon}}{4} + \frac{\sqrt{\left(\frac{a}{2} + \frac{b}{2} - c + \frac{\sqrt{(a-b)^2}}{2}\right)^2 + \varepsilon}}{2} \\ &\approx \begin{cases} a & a \geq b \text{ and } a \geq c \\ b & b \geq a \text{ and } b \geq c \\ c & c \geq a \text{ and } c \geq b \end{cases} \end{aligned} \quad (23)$$

$$\begin{aligned} \Psi_{\min}(a, b, c) &= \frac{a}{4} + \frac{b}{4} + \frac{c}{2} - \frac{\sqrt{(a-b)^2 + \varepsilon}}{4} - \frac{\sqrt{\left(c - \frac{a}{2} - \frac{b}{2} + \frac{\sqrt{(a-b)^2}}{2}\right)^2 + \varepsilon}}{2} \\ &\approx \begin{cases} a & c \geq a \text{ and } b \geq a \\ b & c \geq b \text{ and } a \geq b \\ c & a \geq c \text{ and } b \geq c. \end{cases} \end{aligned} \quad (24)$$

By utilizing the defined differentiable maximum and the minimum operators for the three input values, the MSS theory failure criteria can be redefined in a differentiable form:

$$\text{The MSS theory : } F_{MSS} = \frac{\Psi_{\max}(\sigma_1, \sigma_2, \sigma_3)}{S_y} - \frac{\Psi_{\min}(\sigma_1, \sigma_2, \sigma_3)}{S_y} \leq 1. \quad (25)$$

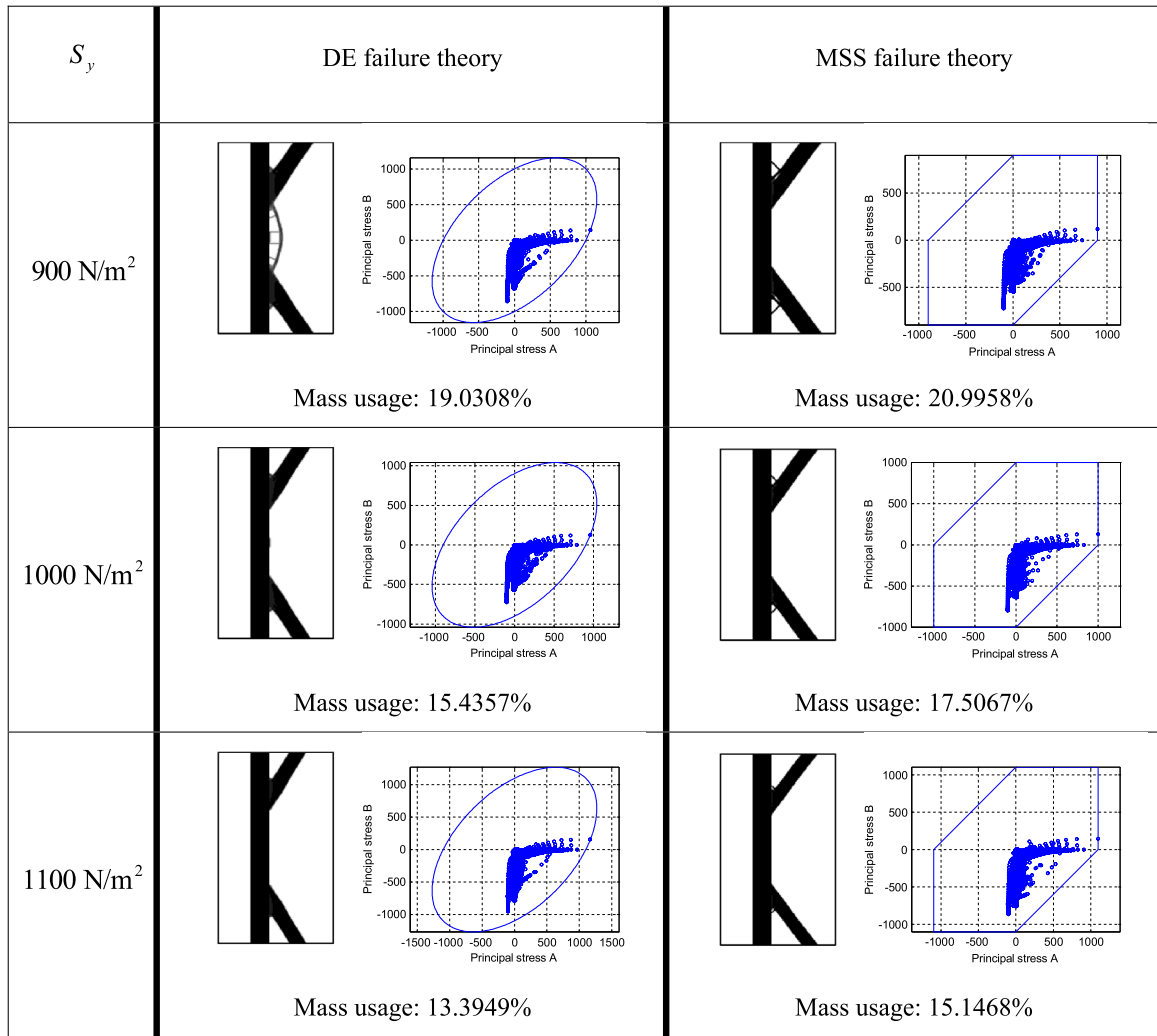


Fig. 12. Optimization results using the DE failure theory and the MSS failure theory (element size: 1.6666×10^{-4} by 1.6666×10^{-4} or mesh: 108×180 , initial design = 1, movelimit = 0.1).

Brittle materials are subject to fail with smaller equivalent strains than ductile materials, and the two static failure criteria, the brittle Coulomb–Mohr (BCM) and ductile Coulomb–Mohr (DCM) theories, are commonly used to determine the potential failure of a structural element. The BCM criterion can be described as follows:

$$F_{BCM_Original}(\sigma) = \frac{\max(\sigma_1, \sigma_2, \sigma_3)}{S_{ut}} - \frac{\min(\sigma_1, \sigma_2, \sigma_3)}{S_{uc}} \leq 1. \quad (26a)$$

With the above differential operators, the following differentiable Coulomb–Mohr formulation is used.

$$\text{Differentiable : } F_{BCM}(\sigma) = \frac{\Psi_{\max}(\sigma_1, \sigma_2, \sigma_3)}{S_{ut}} - \frac{\Psi_{\min}(\sigma_1, \sigma_2, \sigma_3)}{S_{uc}} \leq 1. \quad (26b)$$

The brittle and ductile Coulomb–Mohr criterion

Similar to the BCM criterion, the DCM criterion can be described as follows:

$$F_{DCM_Original}(\sigma) = \frac{\max(\sigma_1, \sigma_2, \sigma_3)}{S_t} - \frac{\min(\sigma_1, \sigma_2, \sigma_3)}{S_c} \leq 1 \quad (27a)$$

$$\text{Differentiable : } F_{DCM}(\sigma) = \frac{\Psi_{\max}(\sigma_1, \sigma_2, \sigma_3)}{S_t} - \frac{\Psi_{\min}(\sigma_1, \sigma_2, \sigma_3)}{S_c} \leq 1. \quad (27b)$$

As the above inequalities are similar to each other with some nominal differences, this research does not distinguish between them. Similar to the maximum shear stress theory, the above criterion uses the max and min operators to define

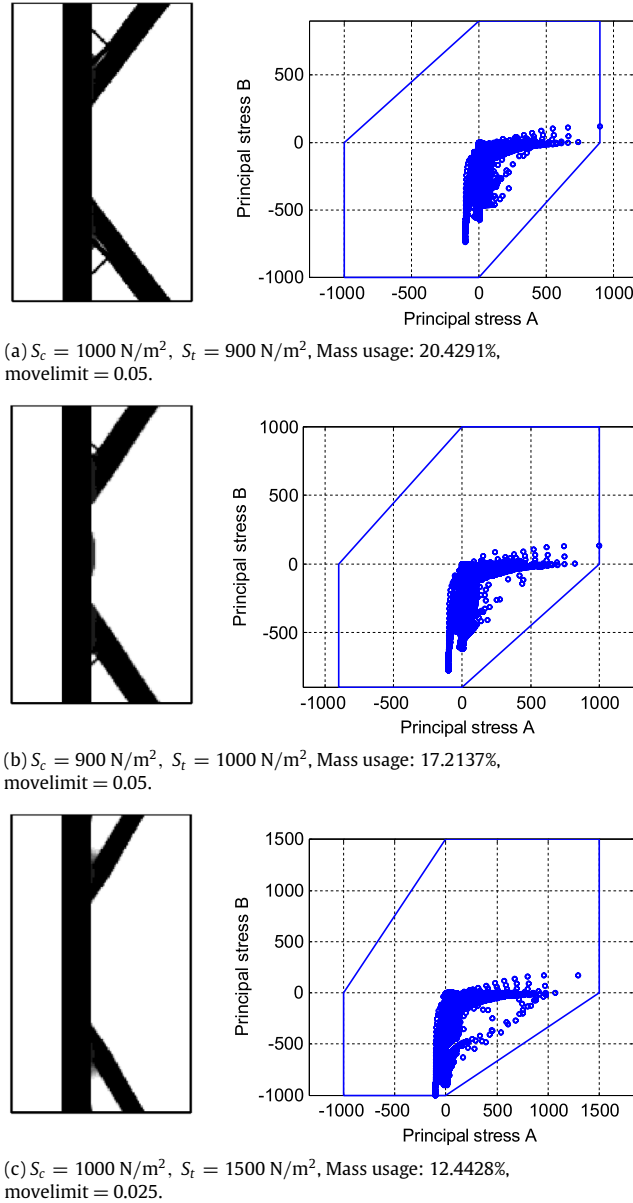


Fig. 13. Optimization results using the CM failure theory (Initial design = 1).

the envelope of the failure region. To make them smooth, the differentiable max and min operators in (23) and (24) should be used.

Drucker–Prager yield criterion (a smooth version of the Coulomb–Mohr criterion)

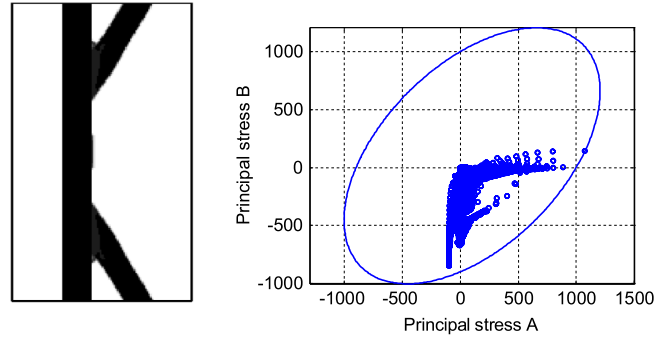
The Drucker–Prager yield criterion is a pressure-dependent failure model for determining whether a material has failed or has exhibited plastic yielding [10,35]. This criterion is introduced to deal with the plastic deformation of rock, concrete, polymers, foams, and other pressure-dependent materials. From a structural optimization point of view, this criterion has been employed to compensate for the failure of brittle materials due to its differentiability with respect to stress components.

The Drucker–Prager yield criterion whose yield surface is a circular cone has the following form.

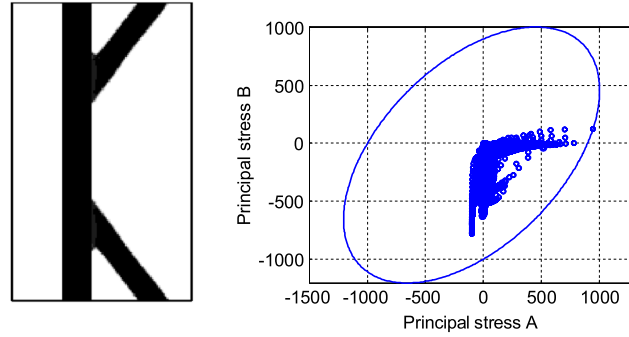
$$F_{DP}(\boldsymbol{\sigma}) = \frac{\alpha I_1(\boldsymbol{\sigma}) + \sqrt{J_2(\boldsymbol{\sigma})}}{H} \leq 1 \quad (28)$$

where the first invariant of the Cauchy stress was defined by I_1 .

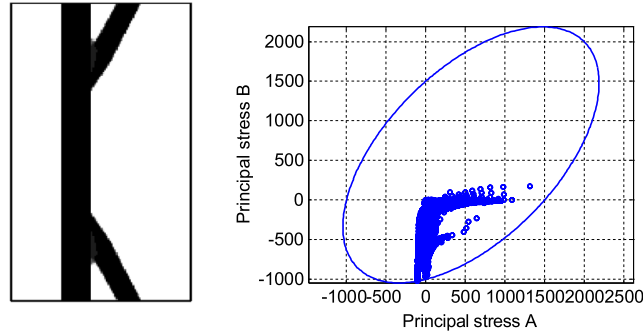
$$I_1(\boldsymbol{\sigma}) = \sigma_{xx} + \sigma_{yy} + \sigma_{zz}. \quad (29)$$



(a) $\sigma_c = 900 \text{ N/m}^2$, $\sigma_t = 1000 \text{ N/m}^2$, Mass usage: 15.9443%, movelimit = 0.05.



(b) $\sigma_c = 1000 \text{ N/m}^2$, $\sigma_t = 900 \text{ N/m}^2$, Mass usage: 16.8442%, movelimit = 0.1.



(c) $\sigma_c = 1000 \text{ N/m}^2$, $\sigma_t = 1500 \text{ N/m}^2$, Mass usage: 12.7712%, movelimit = 0.025.

Fig. 14. Optimization results using the Drucker–Prager failure theory.

The constants α and H are determined experimentally. If the envelope of the Drucker–Prager yield criterion is made to match the outer surface of the Mohr–Coulomb theory, the material constants α and H become:

$$\alpha = \frac{\sigma_c - \sigma_t}{\sqrt{3}(\sigma_c + \sigma_t)}, \quad H = \frac{2\sigma_c\sigma_t}{\sqrt{3}(\sigma_c + \sigma_t)}. \quad (30)$$

3.3. Stress based topology optimization formulation with ductile and brittle failure criteria

The STOM problem minimizing subject volumes to failure constraints for structural forces can be formulated as follows:

$$\begin{aligned} \text{Minimize}_{\gamma} \quad & V(\gamma) = \sum_{e=1}^{NE} \gamma_e v_e \\ \text{subject to} \quad & \langle F_{\max} \rangle^{iter} \leq 1 \end{aligned} \quad (31a)$$

$$\langle F_{\max} \rangle^{iter} \equiv c^{iter} \langle F_{(\bigcirc)} \rangle^{iter}, \quad \bigcirc = DE, MMS, CM \text{ or, } DP \quad (31b)$$

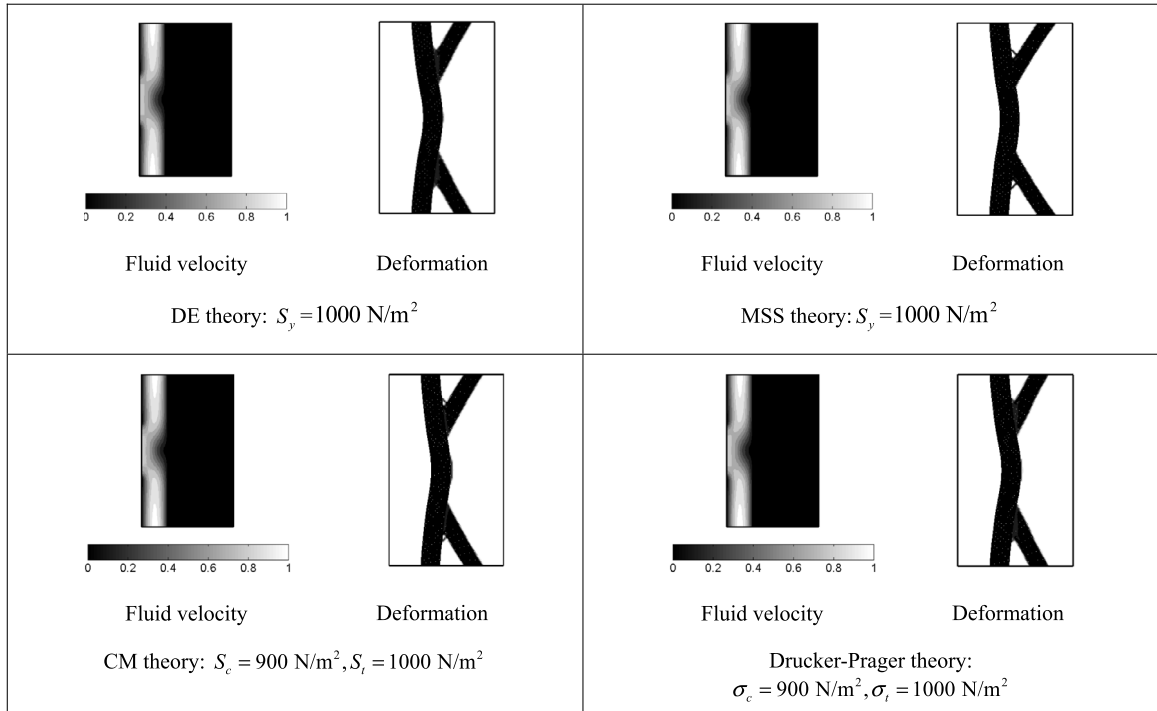


Fig. 15. Fluid velocities and deflection comparison (Deformation scaling: 1, movelimit = 0.1).

$$\langle F_{(\odot)} \rangle^{iter} \equiv \left(\sum_e (F_{(\odot),e})^p \gamma_e \right)^{1/p} \quad (e \in [1, 2, \dots, NE - 1, NE]) \quad (31c)$$

$$c^{iter} = \alpha \frac{F_{(\odot)\max}^{iter-1}}{\langle F_{(\odot)} \rangle^{iter-1}} + (1 - \alpha) c^{iter-1}, \quad (0 < \alpha < 1) \quad F_{(\odot)\max}^{iter-1} = \max_e F_{(\odot),e} \text{ at the } (iter - 1) \text{th iteration} \quad (31d)$$

where the number of design variables is NE . The e th design variable and e th elementary volume are γ_e and v_e , respectively. One aggregated constraint is used in the present optimization formulation. The normalized p -norm maximum failure criterion is $\langle F_{(\odot)} \rangle^{iter}$ and is scaled by the correction factor c^{iter} for F_{\max}^{iter} with the damping factor. The sensitivity analysis is performed by the adjoint variable method. For the sensitivity analysis of the constraint, the sum (zero-order integration) of the failure p -norm constraints multiplied by the design variable at each element is defined ϕ .

$$\langle F_{(\odot)} \rangle^{iter} \equiv \left(\sum_e (F_{(\odot),e})^p \gamma_e \right)^{1/p}, \quad \phi = \sum_e \underbrace{(F_{(\odot),e})^p \gamma_e}_{\phi_e} = \sum_{e=1}^{NE} \phi_e = \underbrace{\int \phi_e dv / \int dv}_{\text{integration order}=0}. \quad (32)$$

Then the following formula are used to for the sensitivity of the function ϕ .

$$\Re(\boldsymbol{\gamma}, \mathbf{V}(\boldsymbol{\gamma}), \mathbf{P}(\boldsymbol{\gamma}), \mathbf{U}(\boldsymbol{\gamma})) = \mathbf{0} \quad (33)$$

$$\begin{aligned} \frac{d\phi}{d\gamma_e} &= \frac{\partial \phi}{\partial \gamma_e} + \left[\frac{\partial \phi}{\partial \mathbf{V}} \frac{\partial \phi}{\partial \mathbf{P}} \frac{\partial \phi}{\partial \mathbf{U}} \right]^T \left[\frac{\partial \mathbf{V}}{\partial \gamma_e} \frac{\partial \mathbf{P}}{\partial \gamma_e} \frac{\partial \mathbf{U}}{\partial \gamma_e} \right] + \boldsymbol{\lambda}^T \left(\frac{\partial \Re}{\partial \gamma_e} + \left[\frac{\partial \Re}{\partial \mathbf{V}} \frac{\partial \Re}{\partial \mathbf{P}} \frac{\partial \Re}{\partial \mathbf{U}} \right]^T \left[\frac{\partial \mathbf{V}}{\partial \gamma_e} \frac{\partial \mathbf{P}}{\partial \gamma_e} \frac{\partial \mathbf{U}}{\partial \gamma_e} \right] \right) \\ &= \frac{\partial \phi}{\partial \gamma_e} + \boldsymbol{\lambda}^T \frac{\partial \Re}{\partial \gamma_e} + \left(\left[\frac{\partial \phi}{\partial \mathbf{V}} \frac{\partial \phi}{\partial \mathbf{P}} \frac{\partial \phi}{\partial \mathbf{U}} \right]^T + \boldsymbol{\lambda}^T \left[\frac{\partial \Re}{\partial \mathbf{V}} \frac{\partial \Re}{\partial \mathbf{P}} \frac{\partial \Re}{\partial \mathbf{U}} \right]^T \right) \left[\frac{\partial \mathbf{V}}{\partial \gamma_e} \frac{\partial \mathbf{P}}{\partial \gamma_e} \frac{\partial \mathbf{U}}{\partial \gamma_e} \right] \\ &= \frac{\partial \phi}{\partial \gamma_e} + \boldsymbol{\lambda}^T \frac{\partial \Re}{\partial \gamma_e} \left(\left[\frac{\partial \phi}{\partial \mathbf{V}} \frac{\partial \phi}{\partial \mathbf{P}} \frac{\partial \phi}{\partial \mathbf{U}} \right]^T + \boldsymbol{\lambda}^T \left[\frac{\partial \Re}{\partial \mathbf{V}} \frac{\partial \Re}{\partial \mathbf{P}} \frac{\partial \Re}{\partial \mathbf{U}} \right]^T = \mathbf{0} \right) \end{aligned} \quad (34)$$

where the velocity, the pressure and the structural displacement vectors of the finite element analysis are \mathbf{V} , \mathbf{P} and \mathbf{U} , respectively and the Lagrange multipliers are $\boldsymbol{\lambda}$. After obtaining the differentiation of the auxiliary function ϕ . The sensitivity of the constraint can be obtained. Furthermore, to consider the regional constraints, we can define the extra variable $\boldsymbol{\xi}$ as shown in Fig. 5.

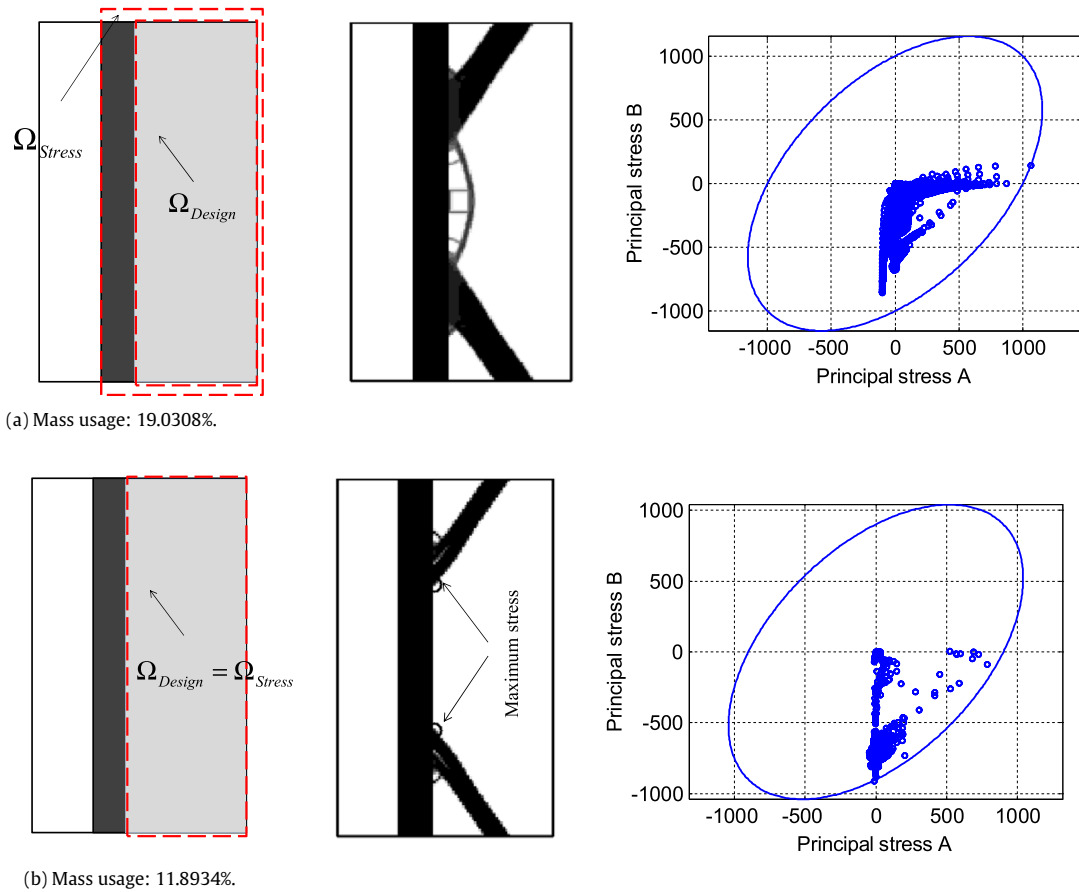


Fig. 16. Effects of the design domain and objective domain (DE theory: $S_y = 900 \text{ N/m}^2$).

In the optimization formulation, we witness the checkerboard patterns showing that the present optimization formulation pursues some stiffer designs in some areas, i.e., not in all areas, constraining the maximum failure constraints. To remove these artificial patterns, generally it is possible to apply the density filter scheme filtering the design variables or the sensitivity values of the objective or the failure constraints for structural problems. The overall procedure is plotted in Fig. 6.

The initial design and the movelimit also play important roles in the above optimization formulation. It is assumed that solid design with ones for the design domain yields a lower possibility of failure. For optimization, the failure constraints are relaxed when considering the maximum principal stress value of solid design. Therefore, some designs uniformly set to 0.5 or 0.3 for the design could violate the failure constraints, and as the optimization process goes by, the constraints could become inactive. If not, the above optimization process ends up with a design that violates the constraint with a large Lagrange multiplier. Sometimes with a smaller initial value for the design variables, the stability of the structural analysis can be sacrificed. In that case, an optimization process with a higher initial value is recommended. In our numerical tests, a constant movelimit strategy between 0.05 and 0.1 was used, and if the objective and constraint values oscillated to the changes of the design variables, a smaller movelimit value or continuous movelimit strategy was employed.

4. Optimization examples

To show the validity of the STOM with brittle and ductile failure criteria for FSI systems, the example section considers several optimization examples with the aforementioned failure constraints. With the assumption of a steady-state laminar fluid–structure interaction, the analysis domains are discretized by Q2-P1 fluidic elements and the first-order structural plane stress elements. For the sensitivity analysis, the adjoint variable method is employed for the global p -norm failure constraint. For the optimizer, the method of moving asymptotes is used [51]. The material properties and boundary conditions of the optimization examples are arbitrarily chosen to show the validity of the present approach.

Example 1. Laminar flow channel problem.

For the first example, the laminar flow channel is considered in Fig. 7. Due to the mechanical stresses caused by the fluid with 240 Reynolds number flowing from the left to the right, the horizontal elastic bar deflects downwards. Then the Y-shape

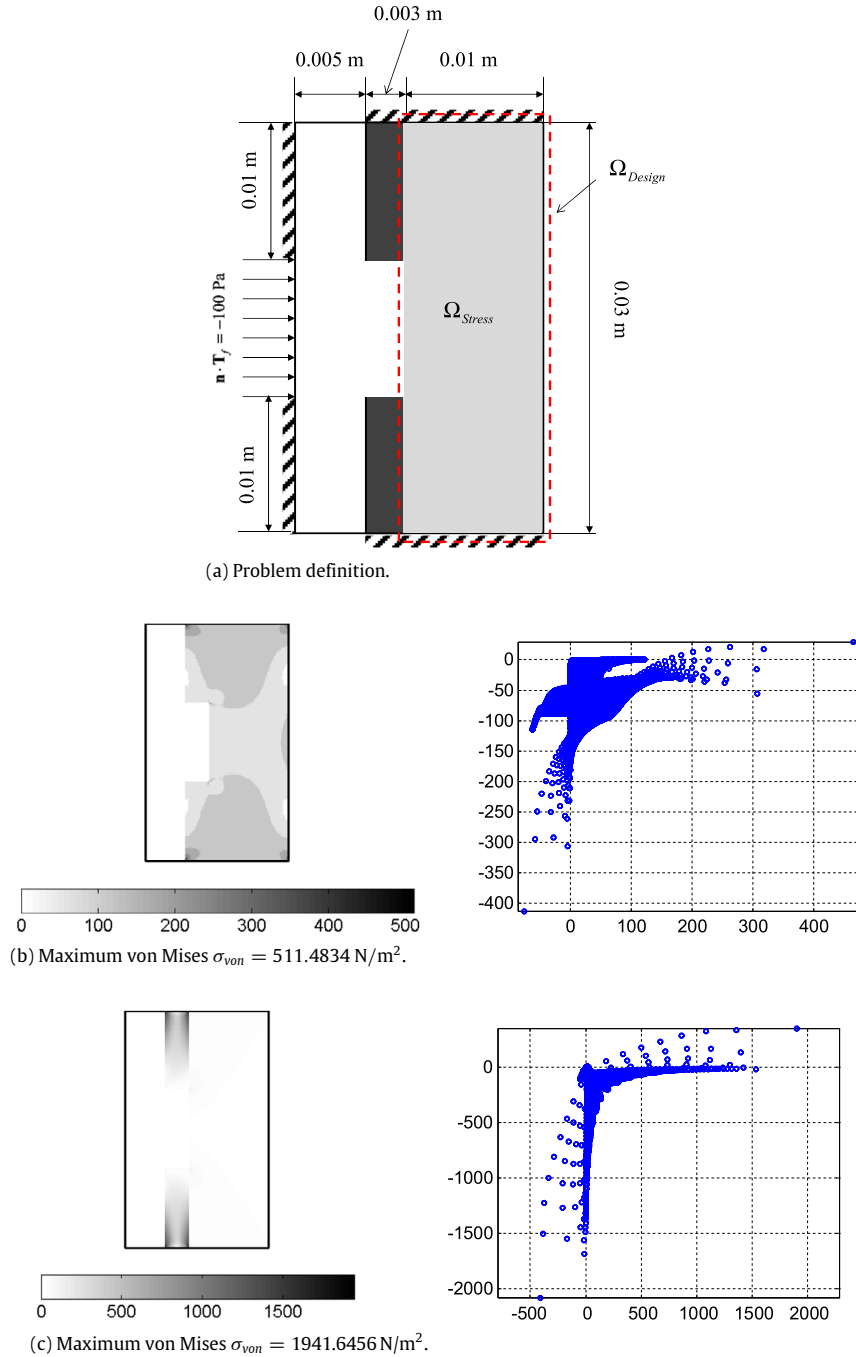


Fig. 17. STOM problem definitions with the pressure input at the center slot on the right (Reynolds number = 5, $\rho = 1000 \text{ kg/m}^3$, $\mu = 1.002 \text{ Pa s}$, $C_s = 10\,000 \text{ N/m}^2$, $\nu = 0.31$, $C_f = C_s \times 10^{-6} \text{ N/m}^2$, $\alpha_{\max} = 10^9$).

structure could be obtained by solving the compliance minimization problem in Fig. 7. The postprocessing of the 5% mass design shows the maximum von Mises stress ($\sigma_{von} = 6.0831 \times 10^6 \text{ N/m}^2$) at the two connection points.

Figs. 8 and 9 show the optimal layouts by solving the STOM problem with $S_y = 6.0 \times 10^6 \text{ N/m}^2$. Compared with the result by the compliance minimization problem in Fig. 7, the straight line designs are obtained. With the STOM problem, the designs with a less mass, i.e. around 1.5% mass percentage, are sufficient to satisfy the stress constraint. However, the compliance values of the STOM designs are approximately 3 times larger than that of the compliance minimization design. The examinations of the deformations in Figs. 8 and 9 reveal that in spite of the similar straight line designs, their roles in supporting the horizontal bar are different.

Fig. 10 shows the optimization histories of the examples.

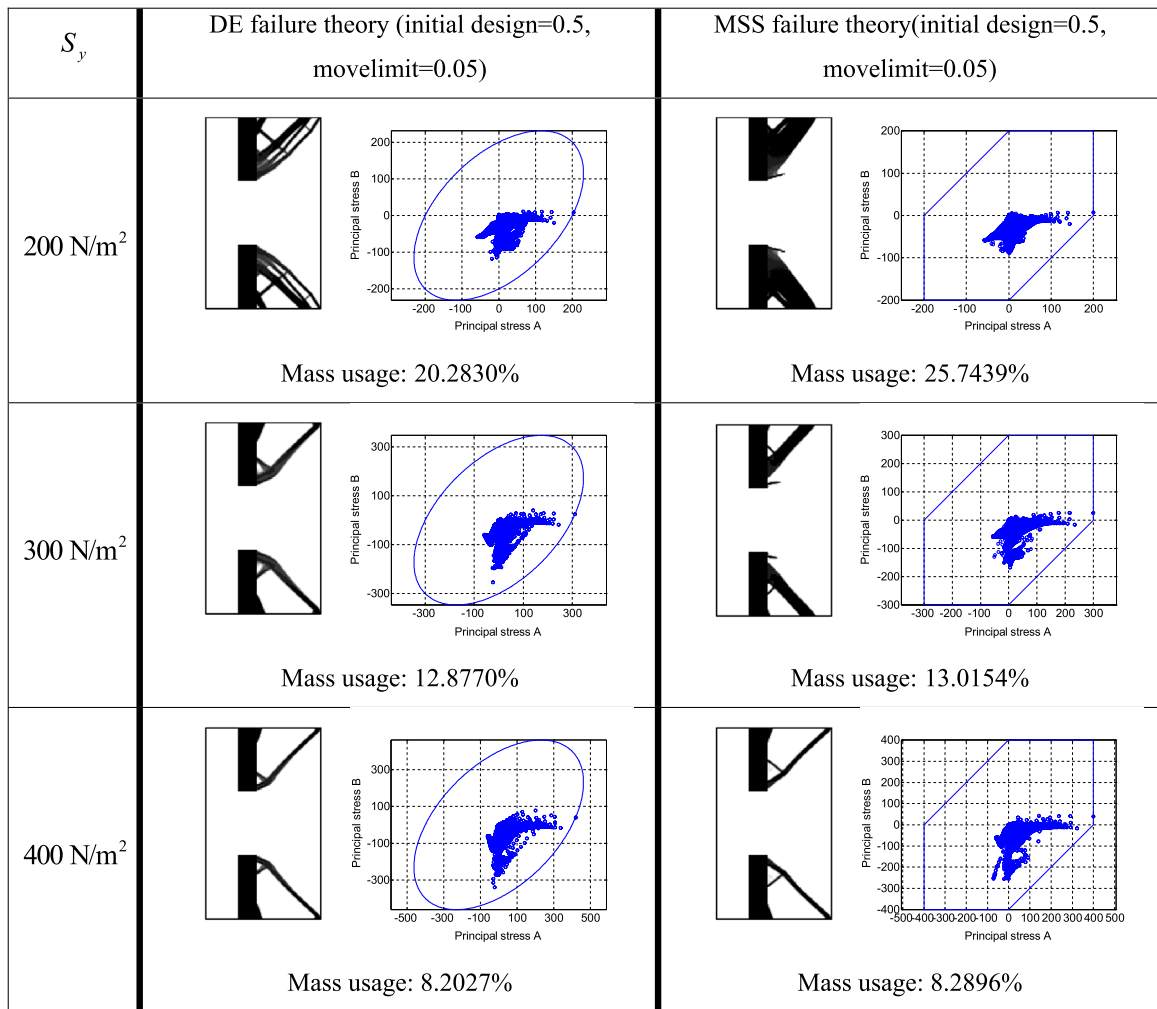


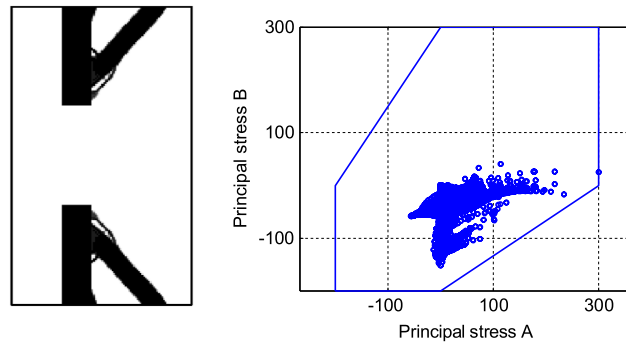
Fig. 18. Optimization results using the DE failure theory and the MSS failure theory (element size: 1.6666×10^{-4} by 1.6666×10^{-4} or mesh: 108×180).

Example 2. Laminar flow channel problem.

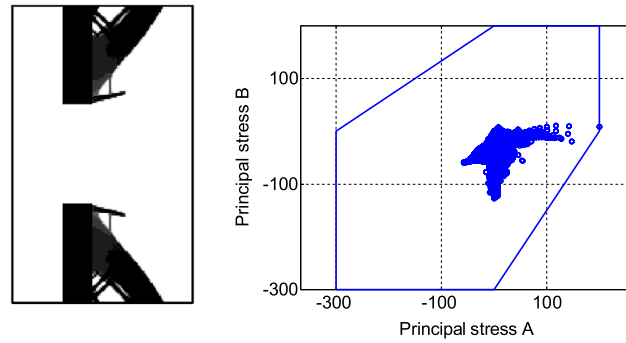
For the next optimization example, a STOM problem is considered in which a thick elastic bar separates the left fluidic domain ($0.001 \text{ m} \times 0.005 \text{ m}$) from the right design domain ($0.03 \text{ m} \times 0.01 \text{ m}$) in Fig. 11(a) [13]. Due to the vertical elastic separator, the fluidic force exerted on the elastic separator is not changed significantly for intermediate design variables.

Fig. 12 shows the local optimal layouts with some allowable stress values for the DE failure theory and the MSS theory. As expected, the two-bar structures supporting the vertical bar can be obtained. With a larger stress limit, the optimal two-bar structures use less mass ratios. The obtained designs with the MSS failure theory with smaller failure envelopes use more mass ratios than the designs with the DE failure theory. For example, with 900 N/m^2 for the maximum tension and compression stress in Fig. 12, 19.0308% mass is used, whereas 20.9958% mass is used with the DE failure theory in Fig. 12. This tendency is observed in the other designs in Fig. 12 with the same maximum stress limits. Secondly, Fig. 13 showed the optimal layouts using the CM failure theory with the different stress limitation values for tension and compression. The similar layouts and the relationships between mass usage and stress limitation values comparing the DE and the MSS failure theories are observed. In Fig. 13(c), with $S_c = 1000 \text{ N/m}^2$, $S_t = 1500 \text{ N/m}^2$, the allowable compression stress is lower than the allowable tension stress. Therefore, the failure region envelope is distorted and the physical locations of the maximum stress points on the edges of the envelope are different from those of the previous optimal layouts. Fig. 14 shows the optimized layouts using the Drucker–Prager. Similar to the CM failure theory designs, the two supporting bars appear with less mass usages than those optimized for the CM failure theory, which is a more conservative theory than the DP failure theory. Unlike the optimal designs of the first example, small differences are observed in their deformations in Fig. 15. It is our opinion that it is due to the symmetric pressure distributions along the vertical non-design domain bar.

Fig. 15 compares the fluid velocities and the deflections of some designs.

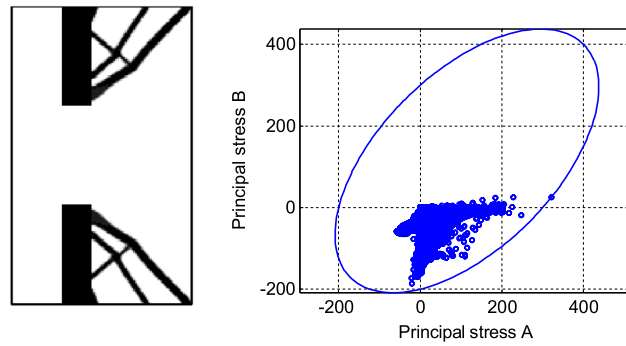


(a) $S_c = 300$, $S_t = 200$, Mass usage: 14.7640%.

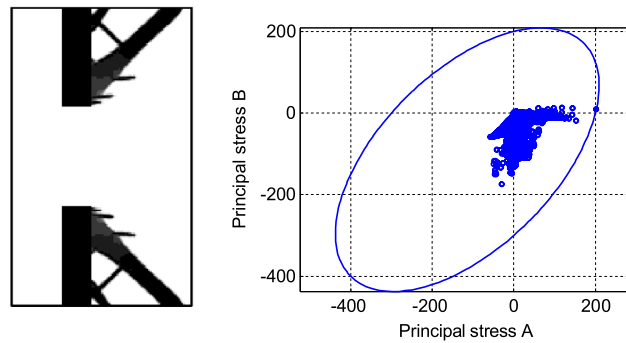


(b) $S_c = 200$, $S_t = 300$, Mass usage: 22.1586%.

Fig. 19. Optimization results using the CM failure theory (initial design = 0.5, movelimit = 0.05).



(a) $\sigma_c = 200$, $\sigma_t = 300$, Mass usage: 13.1234%.



(b) $\sigma_t = 200$, $\sigma_c = 300$, Mass usage: 17.8785%.

Fig. 20. Optimization results using the Drucker–Prager failure theory (initial design = 1, movelimit = 0.1).

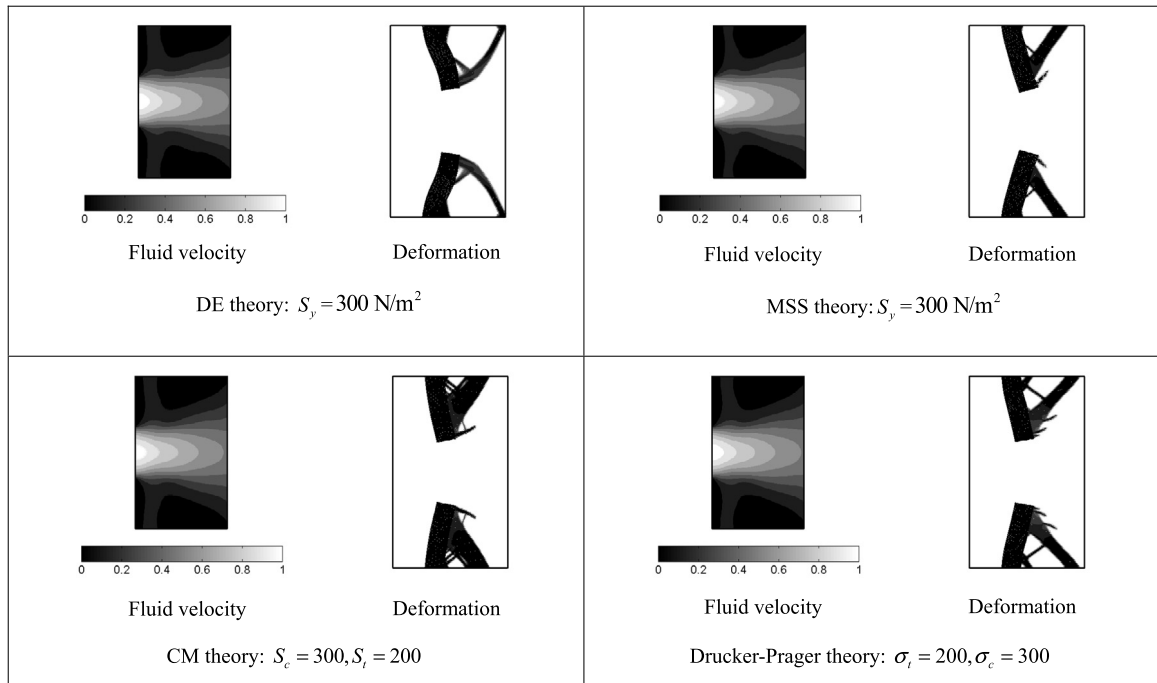


Fig. 21. Fluid velocities and deflection comparison (Deformation scaling: 10).

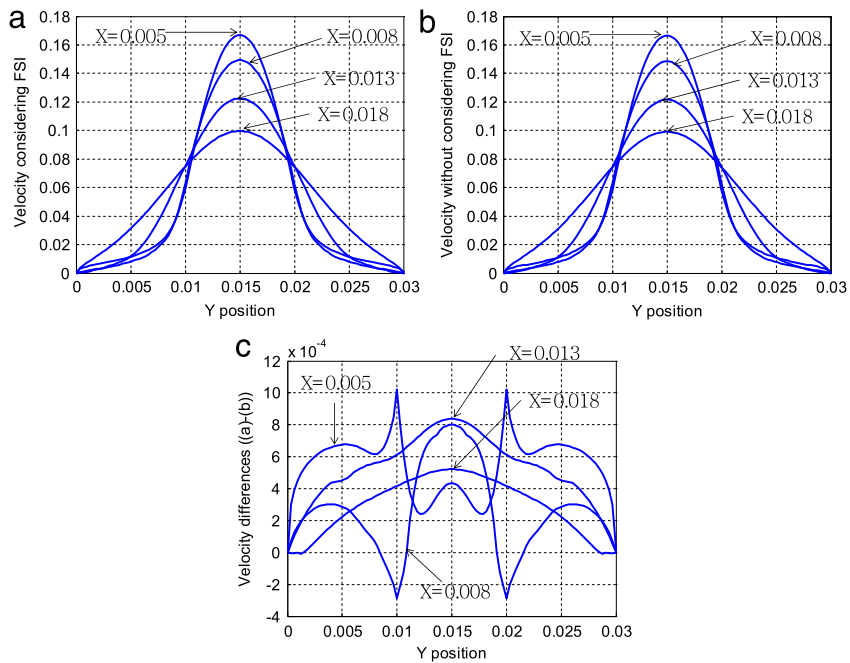


Fig. 22. The fluid velocities with and without fluid–structure interaction. (The design of the DE theory: $S_y = 300 \text{ N/m}^2$ in Fig. 18.)

Design domain effects

Fig. 16 shows the effects of the design domain and objective domain choices. In Fig. 16(a), the objective domain computing the stress values for failure constraints includes the vertical bar. Therefore, as examined before, the maximum stress appears at the corners of the vertical bar. However, in Fig. 16(b), the objective domain excludes the vertical bar and the maximum stress appears at the junctions between the vertical bar and the two supporting bars. Therefore, the different designs in Fig. 16(b) are obtained.

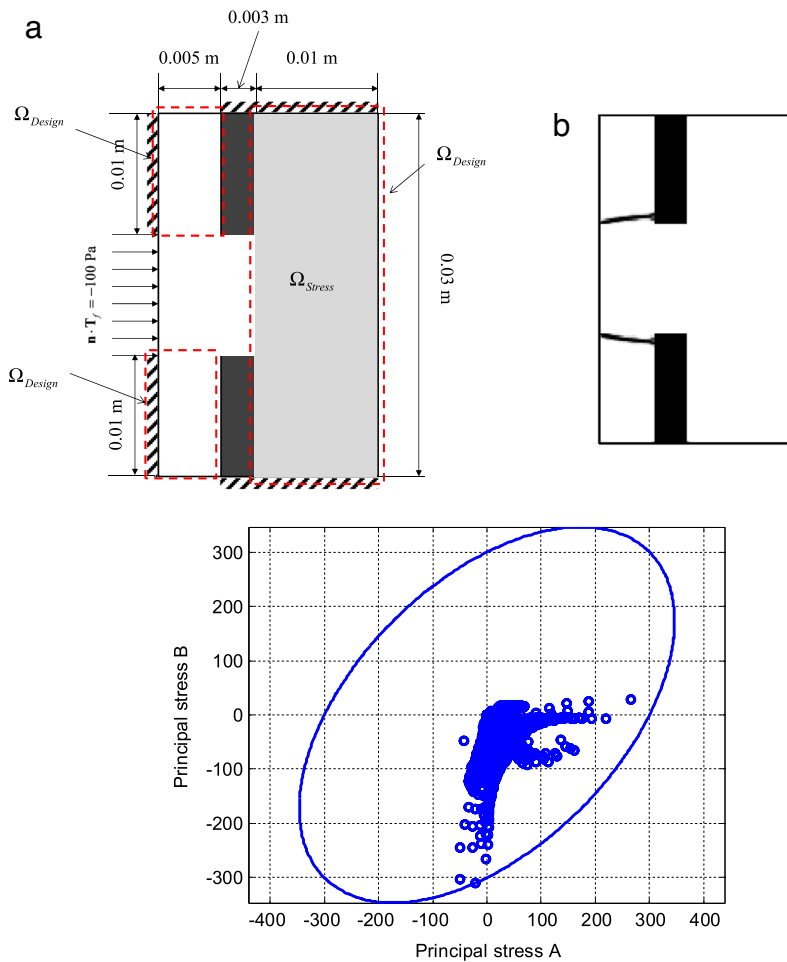


Fig. 23. The design domain effect (the DE theory: $S_y = 300 \text{ N/m}^2$, initial design = 0.5, movelimit = 0.05).

Example 3. Open channel problem.

For the next topology optimization example, a more difficult problem optimizing the interaction boundary between fluids and solids, is considered by setting the middle section of the elastic separator to a fluid as shown in Fig. 11. As the solid bar structure in the second example separates the right domain and the left domain, the fluid forces acting on the surface of the bar-type structure are not significantly altered. Therefore, the von Mises stress inside the objective domain can be easily constrained as one of the characteristics of the second numerical example.

In this example in Fig. 17, depending on intermediate design, fluidic force increases or decreases the magnitude of the von Mises stress, making the global p -norm stress constraint non-monotonically increase or decrease. Therefore, the optimal mutually coupling boundaries, as well as the elastic structure should be designed with the present optimization algorithm. With the present optimization framework, the various optimal layouts of Figs. 18–20 can be obtained; the shapes of the designs are almost similar to each other. The differences in some detail are mainly influenced by the different envelopes and partially due to the local optima issue in topology optimization. In these designs, the elastic structural members only appear behind the upper and lower elastic bars so as not to interrupt the fluidic motion toward the right open channel. As some solid structures between the elastic bars will work as fluid resistance, the cone shape design can be obtained. Fig. 21 compares the fluid velocities and the deflections of some results. Fig. 22 shows the velocity difference of the fluid velocities with and without considering the fluid–structure interaction. As shown, the fluid velocities across the channel become different due to the FSI effect. Note that without considering the FSI structure, the mechanical stresses are not developed.

Fig. 23 shows an optimal design by adding the boxes in front of the rigid bars as the design domain. With this, the thin arc type structures can be obtained rather than a support structure. This example also shows the importance in choosing the design domain.

5. Conclusions

This study develops a new stress-based topology optimization minimizing structural volume subject to failure constraints for ductile and brittle materials for FSI structures. To resolve the interpolation issues of solid and fluid with respect to design variables and interaction boundary issues, the present study adopts the monolithic approach, coupling the Navier–Stokes equation and linear elasticity equation with the deformation tensor. The qp -relaxation method using different penalizations of the SIMP for forward analysis and sensitivity analysis is employed for the singularity issue. In the present approach, the ductile material failure constraints (i.e., the distortion energy theory and maximum shear stress theory) and brittle material failure constraints (i.e., the Drucker–Prager criterion theory and brittle Coulomb–Mohr theory) are employed. Depending on the design domain and boundary condition choice, the interaction boundaries between solids and fluids are subject to change and many local optima exist. In conclusion, this study developed a new STOM problem with various failure constraints while considering fluid–structure interactions with the monolithic analysis method.

Acknowledgment

This work was supported by the National Research Foundation of Korea (NRF) grant funded by the Korea government (MEST) (NRF-2015R1A2A2A11027580) and the Global Frontier R&D Program on Center for Wave Energy Control based on Metamaterials funded by the National Research Foundation under the Ministry of Science, ICT & Future Planning, Korea (No. 2014M3A6B3063711).

References

- [1] F.J. Blom, A monolithic fluid–structure interaction algorithm applied to the piston problem, *Comput. Methods Appl. Math.* 167 (1998) 369–391.
- [2] G.H. Yoon, Topology optimization for stationary fluid–structure interaction problems using a new monolithic formulation, *Internat. J. Numer. Methods Engrg.* 82 (2010) 591–616.
- [3] M. Allen, K. Maute, Reliability-based shape optimization of structures undergoing fluid–structure interaction phenomena, *Comput. Methods Appl. Math.* 194 (2005) 3472–3495.
- [4] E.A. Kontoleon, E.M. Papoutsis-Kiachagias, A.S. Zymaris, D.I. Papadimitriou, K.C. Giannakoglou, Adjoint-based constrained topology optimization for viscous flows, including heat transfer, *Eng. Optim.* 45 (2013) 941–961.
- [5] E.A.K.E.M. Papoutsis-Kiachagias, A.S. Zymaris, D.I. Papadimitriou, K.C. Giannakoglou, Constrained topology optimization for laminar and turbulent flows, including heat transfer, in: *Proc. EUROGEN, Evolutionary and Deterministic Methods for Design, Optimization and Control*, Capua, Italy, 2011.
- [6] E. Oktay, H.U. Akay, O. Merttopcuoglu, Parallelized structural topology optimization and CFD coupling for design of aircraft wing structures, *Comput. & Fluids* 49 (2011) 141–145.
- [7] G.H. Yoon, Topological layout design of electro-fluid-thermal-compliant actuator, *Comput. Methods Appl. Math.* 209 (2012) 28–44.
- [8] B.J. Lee, C. Kim, Automated design methodology of turbulent internal flow using discrete adjoint formulation, *Aerosp. Sci. Technol.* 11 (2007) 163–173.
- [9] Y.D. Ha, S. Cho, Efficient design sensitivity analysis of incompressible fluids using SPH projection method, *Struct. Multidiscip. Optim.* 40 (2010) 307–318.
- [10] Y.J. Luo, Z. Kang, Topology optimization of continuum structures with Drucker–Prager yield stress constraints, *Comput. Struct.* 90–91 (2012) 65–75.
- [11] S.H. Jeong, D.H. Choi, G.H. Yoon, Fatigue and static failure considerations using a topology optimization method, *Appl. Math. Model.* 39 (2015) 1137–1162.
- [12] Y.J. Luo, Z. Kang, Layout design of reinforced concrete structures using two-material topology optimization with Drucker–Prager yield constraints, *Struct. Multidiscip. Optim.* 47 (2013) 95–110.
- [13] G.H. Yoon, Stress-based topology optimization method for steady-state fluid–structure interaction problems, *Comput. Methods Appl. Math.* 278 (2014) 499–523.
- [14] K. Yaji, T. Yamada, M. Yoshino, T. Matsumoto, K. Izui, S. Nishiwaki, Topology optimization in thermal-fluid flow using the lattice Boltzmann method, *J. Comput. Phys.* 307 (2016) 355–377.
- [15] E.M. Dede, Optimization and design of a multipass branching microchannel heat sink for electronics cooling, *J. Electron. Packag.* 134 (2012).
- [16] E.M. Dede, J. Lee, Y. Liu, B. Robert, S.H. Yonak, Computational methods for the optimisation and design of electromechanical vehicle systems, *Int. J. Veh. Des.* 58 (2012) 159–180.
- [17] A.A. Koga, E.C.C. Lopes, H.F.V. Nova, C.R. de Lima, E.C.N. Silva, Development of heat sink device by using topology optimization, *Int. J. Heat Mass Transfer* 64 (2013) 759–772.
- [18] C. Andreasen, O. Sigmund, Saturated poroelastic actuators generated by topology optimization, *Struct. Multidiscip. Optim.* 43 (2011) 693–706.
- [19] C.S. Andreasen, O. Sigmund, Topology optimization of fluid–structure-interaction problems in poroelasticity, *Comput. Methods Appl. Math.* 258 (2013) 55–62.
- [20] J.R.R.A. Martins, J.J. Alonso, J.J. Reuther, High-fidelity aerostructural design optimization of a supersonic business jet, *J. Aircr.* 41 (2004) 523–530.
- [21] G.H. Yoon, Topology optimization for turbulent flow with Spalart–Allmaras model, *Comput. Methods Appl. Math.* 303 (2016) 288–311.
- [22] W. Akl, A. El-Sabbagh, K. Al-Mitani, A. Baz, Topology optimization of a plate coupled with acoustic cavity, *Internat. J. Solids Structures* 46 (2009) 2060–2074.
- [23] M. Bruggi, P. Venini, Topology optimization of incompressible media using mixed finite elements, *Comput. Methods Appl. Math.* 196 (2007) 3151–3164.
- [24] D. Makhija, G. Pingen, R. Yang, K. Maute, Topology optimization of multi-component flows using a multi-relaxation time lattice Boltzmann method, *Comput. & Fluids* 67 (2012) 104–114.
- [25] X. Zhang, Z. Kang, Topology optimization of damping layers for minimizing sound radiation of shell structures, *J. Sound Vib.* 332 (2013) 2500–2519.
- [26] S. Zhou, Q. Li, A variational level set method for the topology optimization of steady-state Navier–Stokes flow, *J. Comput. Phys.* 227 (2008) 10178–10195.
- [27] K. Maute, G.W. Reich, Integrated multidisciplinary topology optimization approach to adaptive wing design, *J. Aircr.* 43 (2006) 253–263.
- [28] X. Guo, W. Zhang, W. Zhong, Stress-related topology optimization of continuum structures involving multi-phase materials, *Comput. Methods Appl. Math.* (2011).
- [29] X. Guo, W.S. Zhang, M.Y. Wang, P. Wei, Stress-related topology optimization via level set approach, *Comput. Methods Appl. Math.* 200 (2011) 3439–3452.
- [30] K.A. James, E. Lee, J.R.R.A. Martins, Stress-based topology optimization using an isoparametric level set method, *Finite Elem. Anal. Des.* 58 (2012) 20–30.
- [31] S.H. Jeong, S.H. Park, D.-H. Choi, G.H. Yoon, Toward a stress-based topology optimization procedure with indirect calculation of internal finite element information, *Comput. Math. Appl.* 66 (2013) 1065–1081.

- [32] J. París, F. Navarrina, I. Colominas, M. Casteleiro, Stress constraints sensitivity analysis in structural topology optimization, *Comput. Methods Appl. Math.* 199 (2010) 2110–2122.
- [33] J. París, F. Navarrina, I. Colominas, M. Casteleiro, Block aggregation of stress constraints in topology optimization of structures, *Adv. Eng. Softw.* 41 (2010) 433–441.
- [34] J. París, F. Navarrina, I. Colominas, M. Casteleiro, Improvements in the treatment of stress constraints in structural topology optimization problems, *J. Comput. Appl. Math.* 234 (2010) 2231–2238.
- [35] S. Amstutz, A.A. Novotny, E.A. de Souza Neto, Topological derivative-based topology optimization of structures subject to Drucker–Prager stress constraints, *Comput. Methods Appl. Math.* 233–236 (2012) 123–136.
- [36] B. Desmorat, Structural rigidity optimization with an initial design dependent stress field. Application to thermo-elastic stress loads, *Eur. J. Mech. A Solids* 37 (2013) 150–159.
- [37] C.-Y. Lin, F.-M. Sheu, Adaptive volume constraint algorithm for stress limit-based topology optimization, *Comput.-Aided Des.* 41 (2009) 685–694.
- [38] S.J. Moon, G.H. Yoon, A newly developed qp-relaxation method for element connectivity parameterization to achieve stress-based topology optimization for geometrically nonlinear structures, *Comput. Methods Appl. Math.* 265 (2013) 226–241.
- [39] M. Bruggi, On an alternative approach to stress constraints relaxation in topology optimization, *Struct. Multidiscip. Optim.* 36 (2008) 125–141.
- [40] M. Burger, R. Stainko, Phase-field relaxation of topology optimization with local stress constraints, *SIAM J. Control Optim.* 45 (2006) 1447–1466.
- [41] M. Bruggi, P. Duysinx, Topology optimization for minimum weight with compliance and stress constraints, *Struct. Multidiscip. Optim.* 46 (2012) 369–384.
- [42] M. Bruggi, P. Venini, A mixed FEM approach to stress-constrained topology optimization, *Internat. J. Numer. Methods Engrg.* 73 (2008) 1693–1714.
- [43] G.D. Cheng, X. Guo, epsilon-relaxed approach in structural topology optimization, *Struct. Optim.* 13 (1997) 258–266.
- [44] M. Stolpe, K. Svanberg, On the trajectories of the epsilon-relaxation approach for stress-constrained truss topology optimization, *Struct. Multidiscip. Optim.* 21 (2001) 140–151.
- [45] M. Bruggi, Topology optimization with mixed finite elements on regular grids, *Comput. Methods Appl. Mech. Engrg.* 305 (2016) 133–153.
- [46] A. Kawamoto, T. Matsumori, T. Nomura, T. Kondoh, S. Yamasaki, S. Nishiwaki, Topology optimization by a time-dependent diffusion equation, *Internat. J. Numer. Methods Engrg.* 93 (2013) 795–817.
- [47] G.Y. Qiu, X.S. Li, A note on the derivation of global stress constraints, *Struct. Multidiscip. Optim.* 40 (2010) 625–628.
- [48] J. París, F. Navarrina, I. Colominas, M. Casteleiro, Topology optimization of continuum structures with local and global stress constraints, *Struct. Multidiscip. Optim.* 39 (2009) 419–437.
- [49] C. Le, J. Norato, T. Bruns, C. Ha, D. Tortorelli, Stress-based topology optimization for continua, *Struct. Multidiscip. Optim.* 41 (2010) 605–620.
- [50] P. Duysinx, M.P. Bendsoe, Topology optimization of continuum structures with local stress constraints, *Internat. J. Numer. Methods Engrg.* 43 (1998) 1453–1478.
- [51] K. Svanberg, The method of moving asymptotes - a new method for structural optimization, *Internat. J. Numer. Methods Engrg.* 24 (1987) 359–373.